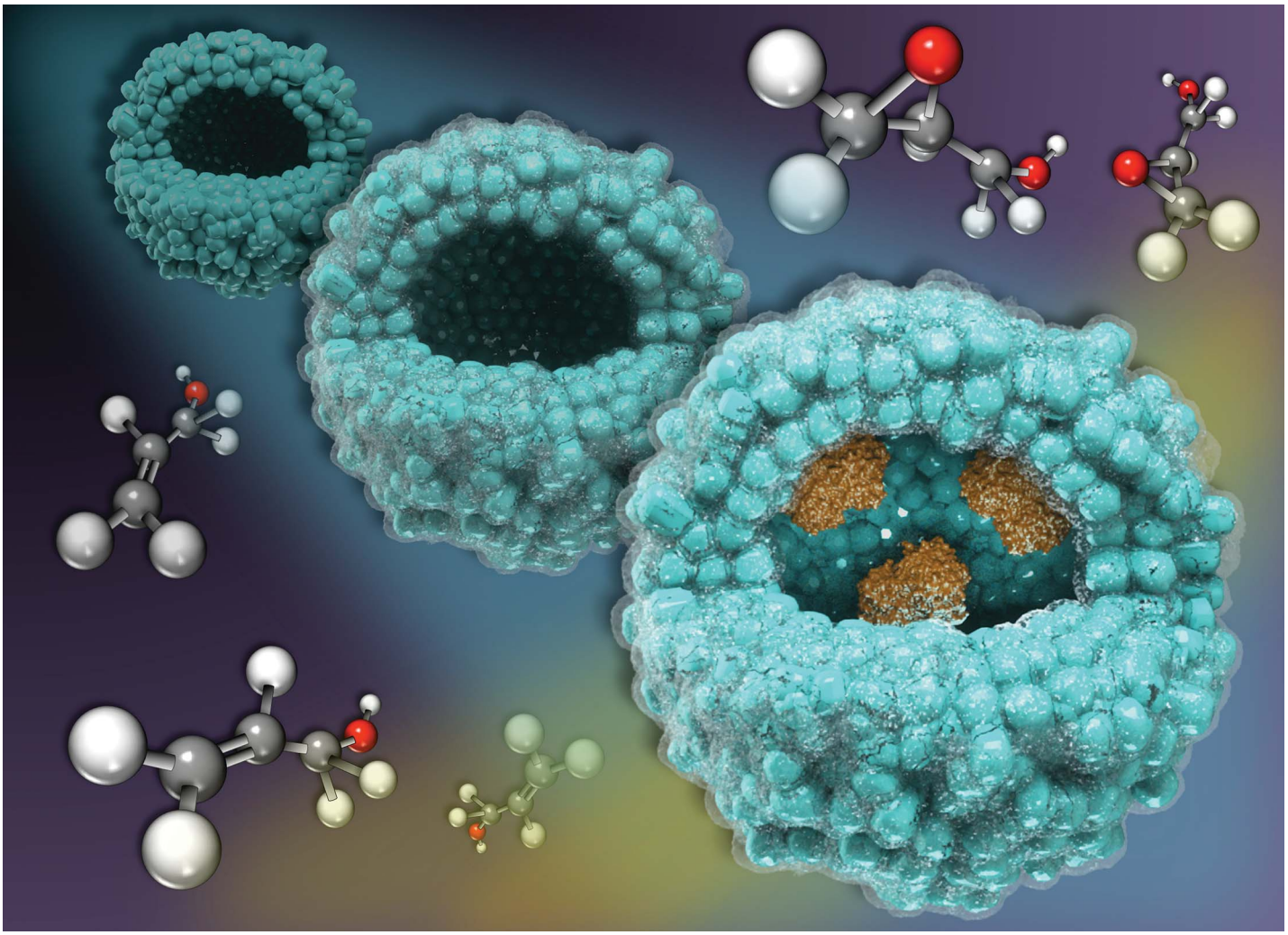

Showcasing research from Professor Damien Debecker's laboratory, Institute of Condensed Matter and Nanosciences, UCLouvain, Belgium.

Hollow zeolite microspheres as a nest for enzymes: a new route to hybrid heterogeneous catalysts

Integrating bio- and chemo-catalytic functionalities on a single solid can allow the revolutionization of the way multistep catalytic reactions can be carried out. However, such integration is not straightforward, for example in the case of zeolite catalysts for which enzyme immobilization is restricted to the external surface. We present a "Lego-like" strategy to tune the enzyme loading inside hollow zeolite microparticles built through a spray drying technique. This approach is a change of the paradigm for enzyme immobilization and could open up new opportunities for the preparation of multifunctional hybrid materials.

As featured in:

See Damien P. Debecker *et al.*, *Chem. Sci.*, 2020, **11**, 954.

ROYAL SOCIETY OF CHEMISTRY

rsc.li/chemical-science

Registered charity number: 207890

Chemical Science

ROYAL SOCIETY OF CHEMISTRY

EDGE ARTICLE

View Article Online
View Journal | View Issue

Cite this: *Chem. Sci.*, 2020, **11**, 954

All publication charges for this article have been paid for by the Royal Society of Chemistry

Hollow zeolite microspheres as a nest for enzymes: a new route to hybrid heterogeneous catalysts†

Valentin Smeets,[a] Walid Baaziz,[b] Ovidiu Ersen,[b] Eric M. Gaigneaux,[a] Cédric Boissière,[c] Clément Sanchez[c] and Damien P. Debecker*[a]

In the field of heterogeneous catalysis, the successful integration of enzymes and inorganic catalysts could pave the way to multifunctional materials which are able to perform advanced cascade reactions. However, such combination is not straightforward, for example in the case of zeolite catalysts for which enzyme immobilization is restricted to the external surface. Herein, this challenge is overcome by developing a new kind of hybrid catalyst based on hollow zeolite microspheres obtained by the aerosol-assisted assembly of zeolite nanocrystals. The latter spheres possess open entry-ways for enzymes, which are then loaded and cross-linked to form cross-linked enzyme aggregates (CLEAs), securing their entrapment. This controlled design allows the combination of all the decisive features of the zeolite with a high enzyme loading. A chemo-enzymatic reaction is demonstrated, where the structured zeolite material is used both as a nest for the enzyme and as an efficient inorganic catalyst. Glucose oxidase (**GOx**) ensures the *in situ* production of H_2O_2 subsequently utilized by the **TS-1** zeolite to catalyze the epoxidation of allylic alcohol toward glycidol. The strategy can also be used to entrap other enzymes or combination of enzymes, as demonstrated here with combi-CLEAs of horseradish peroxidase (HRP) and glucose oxidase. We anticipate that this strategy will open up new perspectives, leveraging on the spray-drying (aerosol) technique to shape microparticles from various nano-building blocks and on the entrapment of biological macromolecules to obtain new multifunctional hybrid microstructures.

Received 12th September 2019
Accepted 9th December 2019

DOI: 10.1039/c9sc04615a

rsc.li/chemical-science

Introduction

Following the green chemistry principles,[1] sustainable synthesis routes are highly sought-after, not necessarily to maximize conversions and yields, but rather to minimize energy consumption and waste production.[2] In this context, the integration of enzymatic and heterogeneous catalysis offers great potential for the development of new industrially relevant cascade processes.[3,4] Examples of such combination are currently flourishing.[5–9] For such chemo-enzymatic reactions, it appears attractive to develop efficient bifunctional hybrid catalysts that combine both the chemo and bio–catalytic activity on the same solid material.[10–12] However, finding a suitable operational window in terms of reaction conditions is challenging because enzymes – unlike most inorganic catalysts – usually work in aqueous conditions under mild conditions of temperature and pH.[13] Importantly, the preparation of an actual chemo-enzymatic heterogeneous catalyst itself is complicated because the two species are often somewhat incompatible. For example, combining a zeolite catalyst with an enzyme in the same multifunctional solid is problematic: zeolite micropores cannot accommodate the enzyme and a covalent grafting on the external surface of the zeolite crystals is ineffective. In the present work, we developed an original synthetic approach allowing to combine an enzyme with a zeolite to form a single chemo-enzymatic heterogeneous catalyst active in a cascade reaction. As a first proof of concept, we focus on a zeolite-catalyzed olefin epoxidation for which the oxidant is produced by an enzyme.

Epoxides belong to an important class of chemical compounds as they are active intermediates for the production of high added value products in the pharmaceutical sector as well as polymers and adhesives.[14] Many epoxidation reactions are run in the liquid phase in the presence of an oxidizing agent and of a solid catalyst, typically a titanosilicate (Ti–SiO_2) – with Ti atoms in tetrahedral coordination in the silica framework.[15] Among the available catalysts and oxidants, titanosilicalite-1 (**TS-1**) and hydrogen peroxide represent the most successful epoxidation processes at the industrial scale. On the first hand, **TS-1** zeolite features tremendous performance for the

[a]*Institute of Condensed Matter and Nanosciences (IMCN), UCLouvain, Place L. Pasteur 1, 1348 Louvain-la-Neuve, Belgium. E-mail: damien.debecker@uclouvain.be*
[b]*Institut de Physique et Chimie des Matériaux de Strasbourg (IPCMS), UMR 7504 CNRS – Université de Strasbourg, 23 rue du Loess, 67034 Strasbourg Cedex 2, France*
[c]*Laboratoire Chimie de la Matière Condensée de Paris (LCMCP), Sorbonne Université, CNRS, Collège de France, PSL Research University, 4 Place Jussieu, F-75005 Paris, France*

† Electronic supplementary information (ESI) available: Detailed experimental procedures, additional figures, detailed description of the mathematical model. See DOI: 10.1039/c9sc04615a

epoxidation of lower olefins (*e.g.* propylene, allyl alcohol, allyl chloride, *etc.*),[16] even in water and at moderately low temperature. On the second hand, hydrogen peroxide is considered as one of the greenest oxidants, since it produces water as the only by-product. However, industrially, H_2O_2 is currently produced *via* a non-green and centralized anthraquinone-based process.[17] H_2O_2 is also intrinsically unstable: transportation and storage of peroxo compounds have been the cause of important damage in the chemical industry.

As an alternative, H_2O_2 could be produced *in situ* by an enzyme, such as glucose oxidase (**GOx**, E.C 1.1.3.4), using molecular oxygen and β-D-glucose as bio-sourced and renewable substrates.[18] Immobilizing the enzyme onto a solid support (*e.g.* by adsorption, covalent binding, encapsulation)[19–21] usually allows stabilizing the enzyme against heat and organic solvents as well as to recover it at the end of the reaction.[22,23] Additional motivations for enzyme immobilization include the perspective of performing enzymatic reactions in continuous flow processes[24,25] and implementing multi-enzymatic cascade reactions.[26,27]

Moving further, we aim at developing a hybrid chemo-enzymatic catalyst by combining the enzyme with a carrier that is itself catalytically active. Such hybrid catalyst – combining both the activity of a heterogeneous catalyst and of an enzyme in a single reusable solid – would be very attractive for various one-pot tandem catalytic systems[3,28,29] where one reaction is carried out by an inorganic catalyst and the other one is catalyzed by an enzyme. However, only very few studies report such true hybrid heterogeneous catalysts showing a chemo-enzymatic activity.[30–33] In 2010, Vennestrøm *et al.* proposed the chemo-enzymatic formation of epoxides by tandem catalysis using free **GOx** and **TS-1** zeolite (Scheme 1).[31] The direct immobilization of the enzyme on the surface of the microporous **TS-1** *via* covalent anchoring was also attempted but the epoxide production was limited to traces, due to the low enzyme loading, and to the poor enzyme stability against experimental conditions. In fact, **TS-1** possesses a low external surface area and a low silanol content that limit the number of anchoring sites for the enzyme.

A first way to increase the enzyme loading could be to immobilize it onto a Ti–SiO_2 epoxidation catalyst possibly prepared by a bottom-up sol–gel approach to generate larger pores.[34,35] Such mesostructured materials may possess a much larger accessible surface area for the enzyme coupled with a higher silanol content, allowing to increase the enzyme loading. Yet, in the presence of water (which is required for the enzyme) such amorphous mixed oxides rapidly deactivate.[36,37] Therefore, **TS-1** zeolite should be preferred as host for the enzyme, since the crystallinity and intrinsic hydrophobicity of this material protect the Ti active sites against deactivation when carrying out reaction in aqueous conditions.[38] However, the microporosity of **TS-1** limits the enzyme loading to the external surface, falling into a dilemma. A possible solution could be to use large hollow zeolite crystals[39] as cargos to load large amounts of enzyme; yet these structures do not offer entry ways for enzymes to be loaded in the central cavity.

Here, we propose a new strategy (Scheme 2) for the preparation of a hybrid catalyst that allows to combine all the features of the zeolite (**TS-1**) with a high loading of enzyme (**GOx**). The method is based on the aerosol-assisted[40–42] assembly of **TS-1** nanocrystals to form hollow zeolite microspheres with a hierarchical porosity and high epoxidation activity in water-based media. Hierarchical zeolites[43–50] have already been identified as possible candidates for enzyme immobilization[51,52] but never exploited in chemo-enzymatic catalysis. The presented aerosol method allows preparing hierarchical hollow zeolite structures using an easy, continuous, and scalable aerosol process.[53] The spheres can be loaded with the enzymes which are then cross-linked[54,55] to secure their entrapment and avoid their subsequent leaching.[56,57] Thus, the hollow microspheres are used both as epoxidation catalysts and as vessels for the enzyme. More importantly, we demonstrate that this material synthesis strategy allows to easily tune the enzyme loading, thereby providing a versatile method to envisage the one-pot production of valuable molecules. The strategy can also be used to entrap other enzymes and combinations of enzymes, which paves the way to more intricate chemo-enzymatic cascade processes.

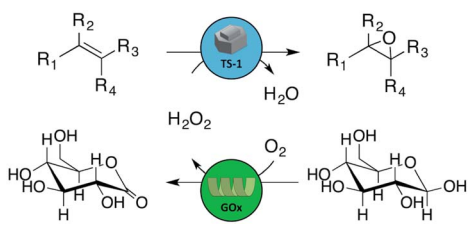

Scheme 1 Reaction pathway for the chemo-enzymatic combination of glucose oxidase (**GOx**) and inorganic **TS-1** epoxidation catalyst (**TS-1**) with *in situ* production of H_2O_2. In the present work, the zeolite (blue) and the enzyme (green) are combined in a single bifunctional catalyst.

Results and discussion

The inorganic catalyst – called "**TS-1_Aer**" – was prepared by an aerosol technique from a **TS-1** colloids suspension[58] (*ca.* 10 wt%) and a clear silica precursor solution containing a Si precursor as well as pluronic F127 and tetrapropylammonium cations (TPA^+) templates. As depicted in Scheme 2a, the **TS-1** suspension supplemented with Si precursor and with templates is sprayed in the form of an aerosol and dried rapidly upon contact with a flow of hot air (experimental details can be found in the ESI†). The two mixtures were mixed so that the final composition of the solid material is 50 vol% **TS-1** and 50 vol% porous silica. As a reference material, **TS-1** nanocrystals were isolated by centrifugation of the 10 wt% suspension, followed by drying in air and calcination. This reference catalyst is denoted "**TS-1**". ICP-AES analysis showed that the experimental bulk Ti content (mol Ti/(mol Ti + mol Si) × 100%) of **TS-1** was 1.5%, close to the nominal one (1.8%). Owing to the additional presence of the silica binder, the Ti content in **TS-1_Aer** was lower (1.1%).

XPS analyses were conducted in order to investigate the surface composition and to probe the quality of the Ti

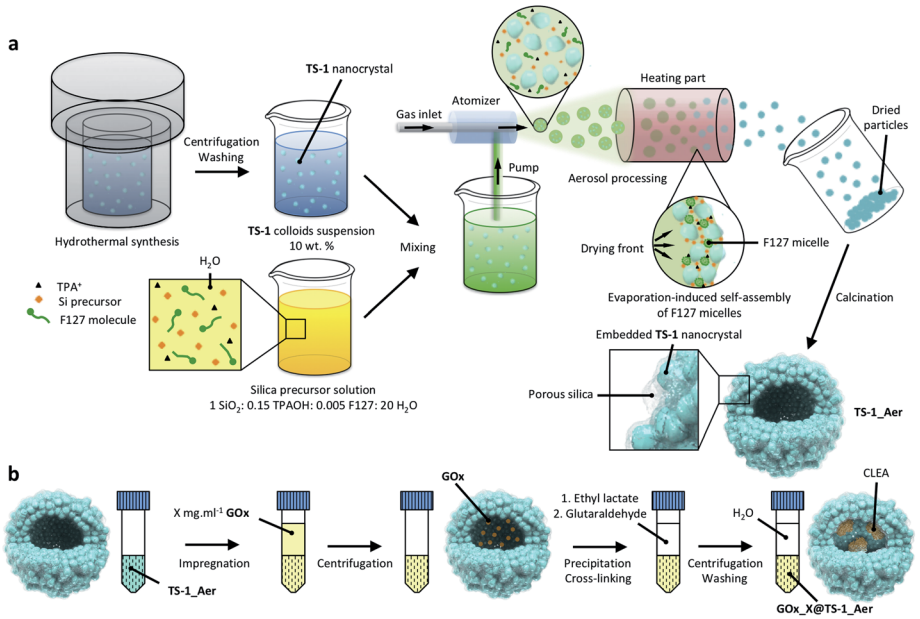

Scheme 2 Schematic representation of the synthesis strategy used for (a) the preparation of hollow zeolite microspheres formed by the aggregation of TS-1 crystals using the aerosol method, (b) the immobilization of glucose oxidase on the aerosol-made material by the formation of entrapped cross-linked enzyme aggregates (CLEAs).

dispersion. In **TS-1**, the surface Ti content was 1.3%, close to the bulk composition. From the Ti $2p_{3/2}$ peak decomposition[59,60] (Fig. S7, ESI†), only 10% of the total Ti content is imputable to extra-framework Ti–O–Ti (458.5 eV) whereas a large majority of Ti species formed Ti–O–Si oxo-bridges (460.0 eV). The maximum absorption band at *ca.* 220 nm in the DRUV-vis spectrum of **TS-1** indicates that these dispersed species are in a tetrahedral coordination sphere (Fig. 1a).[61] The latter 4-coordination sites are known to be the active species in epoxidation.[38] From the minor contribution above 250 nm and the data from XPS, we surmise that the small amount of extra-framework Ti species – with higher coordination numbers (5- and 6-) – were incorporated in the form of oligomeric Ti species or amorphous TiO_2 nano-domains.[62] However, no evidence of the presence of a TiO_2 crystalline phase, such as anatase – having a characteristic absorption band at *ca.* 330 nm[63] – was found. This observation was further supported by the PXRD pattern of **TS-1**, which did not show the signature peak of anatase at *ca.* 25° (Fig. 1b).[64]

In **TS-1_Aer**, Ti atoms were still detected at the solid surface by XPS, although the signal from Ti electrons was partially masked by the surrounding silica phase (Fig. S7†). DRUV-vis spectrum of **TS-1_Aer** is analogous to that of **TS-1** (Fig. 1a). Similar to **TS-1**, **TS-1_Aer** presented the typical MFI crystal structure[58] measured by PXRD analysis (Fig. 1b). Those results confirmed that both Ti speciation and crystallinity of **TS-1** were well preserved after the aerosol processing.

SEM-FEG images (Fig. 2a and b, see also Fig. S8†) show that single particles of **TS-1_Aer** – with size in the 0.5–8 μm range (Fig. S9†) – display a spherical shape. Embedded **TS-1** crystals – with individual dimension of 100–150 nm – are visible at the surface along with the porous silica phase, showing pore size of *ca.* 10 nm (inset Fig. 2b) as well as interparticular voids between **TS-1** crystals – with a mean size of 40–60 nm. Such results were confirmed by STEM Electron Tomography experiments realized on representative **TS-1_Aer** particles of *ca.* 3 μm and *ca.* 1.2 μm (Fig. 2c–e and S10,† respectively). Fig. 2d presents a typical (*xy*) slice extracted from the 3D volume, (Fig. 2d) which shows

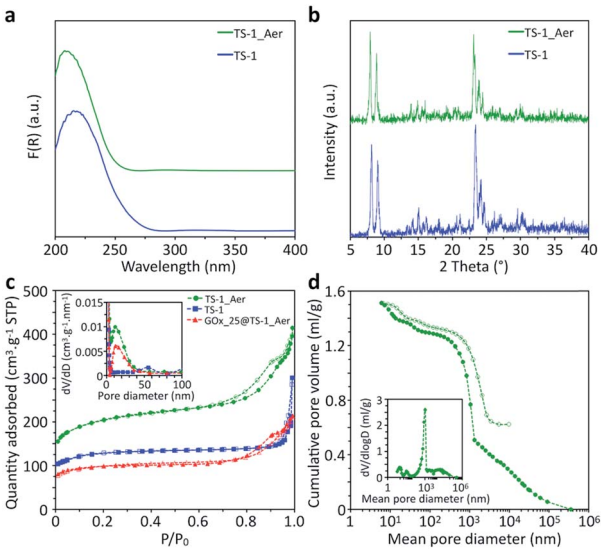

Fig. 1 (a) DRUV-vis spectra ($F(R)$ is the Kubelka–Munk Function) and (b) PXRD patterns of **TS-1** and **TS-1_Aer**, (c) N_2 adsorption–desorption isotherms of the **TS-1**, **TS-1_Aer** and **GOx_25@TS-1_Aer** catalysts, (d) Hg intrusion–extrusion isotherms of **TS-1_Aer**. Pore size distributions (PSDs) based on the adsorption/intrusion branch are shown in inset. Full symbols are used for the adsorption/intrusion isotherms and empty symbols are used for the desorption/extrusion isotherms.

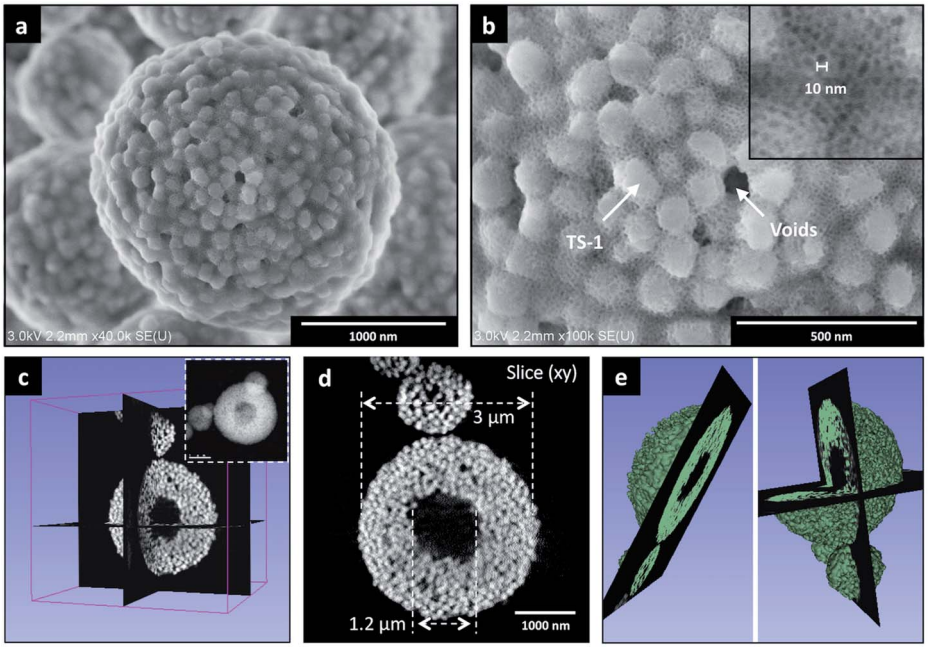

Fig. 2 (a) SEM-FEG image of **TS-1_Aer**, (b) magnified image showing **TS-1** crystals and *ca.* 10 nm mesopores from the porous silica phase (inset). Additional SEM-FEG images are presented in Fig. S8.† (c) 3D volume reconstructed by STEM Electron Tomography of one **TS-1_Aer** particle of *ca.* 3 µm in size (present inset), (d) typical (*xy*) slice extracted from the 3D volume illustrating the presence of a central cavity and (e) the corresponding 3D model (video animation available in ESI†).

clearly the hollow character of a catalyst particle of *ca.* 3 µm (3D model animation is available in ESI†). The central void part was found to be about 1.2 µm in diameter (and about 400 nm for the particle of *ca.* 1.2 µm, Fig. S10c†). The porous silica shell is formed by individual crystals displaying a faceted morphology with a mean size of *ca.* 120 nm, consistent with the initial size of the **TS-1** zeolite nanocrystals (Fig. S10d†).

N_2 adsorption–desorption isotherms of **TS-1** and **TS-1_Aer** are shown in Fig. 1c, along with the adsorption pore size distributions (PSDs). As expected, **TS-1** solely displays micropores ($V_\mu = 0.15$ cm^3 g^{-1}) and interparticular voids which contribute to the total pore volume ($V_P = 0.43$ cm^3 g^{-1}). For this material, the external specific surface area is 130 m^2 g^{-1} according to the *t*-plot method (Fig. S11†). In comparison, a pore volume of 0.58 cm^3 g^{-1} (with $V_\mu = 0.18$ cm^3 g^{-1}) is obtained for **TS-1_Aer** and the external specific surface area reaches 320 m^2 g^{-1}. This is associated with the presence of mesopores in the silica binder, as also evidenced by the shape of the type IV isotherm (see Fig. 1c). Adsorption PSD in Fig. 1c confirms the presence of mesopores in the 10–20 nm range. This pore size is related to the templating effect of F127 micelles, swollen due to the additional incorporation of TPA^+ cations.[35,65] Thus the shell of the hollow spheres is porous enough to allow for the diffusion of individual **GOx**, whose size is $6.0 \times 5.2 \times 7.8$ nm^3.[66]

To have a better insight into the macroporosity of the aerosol-made catalyst, a Hg porosimetry experiment was carried out. The inset of Fig. 1d shows two contributions at 10 and 40 nm, which are in agreement with data from the N_2 physisorption analysis (Fig. 1c) and SEM-FEG images (inset of Fig. 2b), respectively. The intrusion isotherm shows also an increase of the cumulative pore volume corresponding to pore diameters between 0.3 and 1.5 µm, which can be assigned to the hollow interior of the spheres, as also indicated by the STEM Electron Tomography experiments (Fig. 2d and S10c†). Interstices derived from the packing of the spheres are most likely found in the region between 1 and 10 µm, and represent approximately 26% of the intrusion volume according to the Mayer–Stowe model.[67] Combining data from N_2 physisorption and Hg porosimetry, the total pore volume – taking into account the three levels of micro-, meso- and macro-porosity – was *ca.* 1.3 cm^3 g^{-1}.

The catalytic performance of **TS-1_Aer** for the Ti-catalyzed conversion of allyl alcohol in water (45 °C) was compared to **TS-1**. A hot filtration test was carried out, confirming that all the activity was attributable only to the solid (Fig. S12†). The catalytic activity of **TS-1_Aer** (approximated by the kinetic constant *k* calculated by an initial rate analysis, Fig. 3a) is lower than that of **TS-1**. However, after normalization by the amount of **TS-1** crystals to account for the presence of the silica binder (mass fraction of **TS-1** in the materials is *ca.* 80 wt%), the two catalysts were shown to have roughly the same specific rate constant (*ca.* 2.5×10^{-5} s^{-1} ($g_{TS\text{-}1}$ L^{-1})), showing that the intrinsic activity of **TS-1** crystals in **TS-1_Aer** is fully preserved. This is correlated with the fact that the Ti speciation and catalyst crystallinity are completely maintained after aerosol processing. Besides, like **TS-1**, **TS-1_Aer** remained fully selective toward the epoxide product (no formation of glycerol after 3 h of reaction). A recyclability study showed that the activity was preserved over three consecutive tests (Fig. 3b).

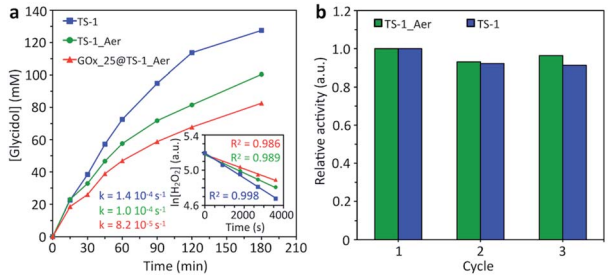

Fig. 3 (a) Kinetic data for the Ti-catalyzed conversion of allyl alcohol into glycidol in H_2O using aq. 30 wt% H_2O_2 as oxidizing agent. In inset is shown the corresponding initial rate analysis, (b) recyclability study of the **TS-1** and **TS-1_Aer** catalysts. Data were collected in the initial stage of the reaction (45 min reaction time) and the catalytic activity (expressed in terms of glycidol production per g of catalyst) relative to the first test was calculated for each catalyst. Experimental conditions: $T = 45$ °C, [CATA] = 5 g L^{-1}, [allyl alcohol] = 0.9 M, [H_2O_2] = 0.18 M.

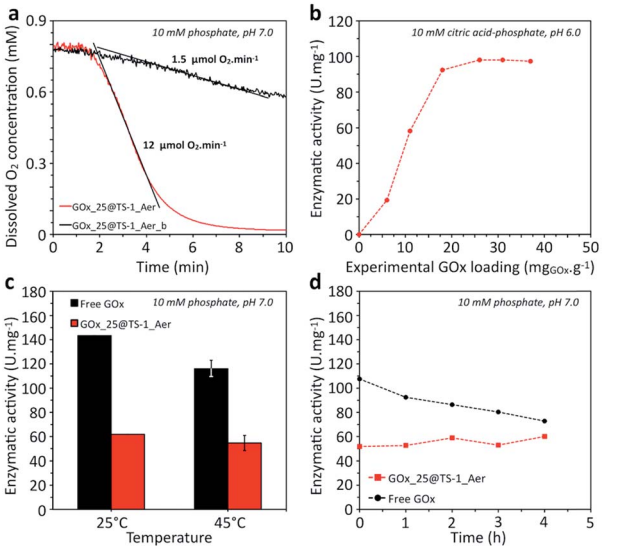

Fig. 4 (a) Kinetic data for the **GOx** catalyzed consumption of oxygen using **GOx_25@TS-1_Aer** and **GOx_25@TS-1_Aer_b** (5 mg of solid catalyst in 50 mL), (b) comparison of the specific enzymatic activity in hybrid catalysts prepared with various enzyme loadings, (c) comparison of the specific enzymatic activity of free and immobilized **GOx** at 25 and 45 °C; the error bars represent standard deviations and are calculated on a triplicate, (d) stability against time at 45 °C of free and immobilized **GOx**. Experimental conditions: $T = 45$ °C, [D-glucose] = 200 mM. The specific enzymatic activity is expressed in U mg^{-1}; the mass of **GOx** in the hybrid catalyst is deduced from the experimental enzyme loading.

The enzyme was entrapped in **TS-1_Aer** *via* an impregnation-precipitation-cross-linking method, leading to the formation of cross-linked enzyme aggregates (CLEAs)[68] inside of the hollow sphere particles (Scheme 2b, see also the detailed experimental procedure in ESI†). In this procedure, ethyl lactate is used as a precipitating agent, forcing the enzyme molecules to come closer to each other in the microparticles and allowing an efficient cross-linking upon the subsequent addition of glutaraldehyde. The obtained hybrid bifunctional catalyst was denoted "**GOx_X@TS-1_Aer**", where *X* stands for the concentration of the enzymatic solution used during the impregnation step (in mg mL^{-1}). The volume of solution that was used to impregnate the solid particles after elimination of the excess by centrifugation was in the 1.3–1.4 $cm^3\ g^{-1}$ range, which is very close to the cumulative pore volume of *ca.* 1.3 $cm^3\ g^{-1}$ estimated by N_2-physisorption and Hg porosimetry. We therefore surmise that only a small fraction of the impregnation solution filled the interstitial voids between the packed spheres while most of the enzymes were inside the microsphere cavities (see below).

In the range of enzyme concentrations tested (*i.e.* 2.5–25 mg mL^{-1}) – corresponding to nominal enzyme loadings of 5–50 $mg_{GOx}\ g^{-1}$ (one example of calculation is given in ESI†) – the immobilization yield was between 75 and 100%, as illustrated in Fig. S13.† This result shows that the final enzyme loading can be simply controlled by choosing the enzyme concentration in the solution. For example, the enzyme loading in **GOx_25@TS-1_Aer** was 37 $mg_{GOx}\ g^{-1}$ (*vs.* 50 $mg_{GOx}\ g^{-1}$ nominal loading). As a comparison, the enzyme loading in a material prepared without precipitation and cross-linking agents (**GOx_25@TS-1_Aer_b**, see ESI†) was 6 $mg_{GOx}\ g^{-1}$ only, showing that most of the enzyme was lost in the washing fractions in this case (Bradford assay). This result is a strong evidence of the major role of the precipitation and cross-linking steps on the heterogeneization of the enzyme and thus on the enzymatic activity of the hybrid material. Indeed, the curves in Fig. 4a show a *ca.* 8 times higher activity for **GOx_25@TS-1_Aer** compared to **GOx_25@TS-1_Aer_b**, consistent with the lower enzyme loading in the latter material. A filtration test on **GOx_25@TS-1_Aer** showed that more than 99% of the enzymatic activity could be assigned to the solid (Fig. S14†). Also, no leaching was detected even after prolonged storage of the catalyst, as verified by a Bradford test.

As opposed to the scenario where the enzyme would be grafted at the external surface of the zeolite, our method offers high flexibility in terms of enzyme loading because the loading can be tuned simply by adapting the enzyme concentration in the impregnation step. The hybrid catalysts prepared with various loadings of **GOx** reached different levels of specific enzymatic activity (Fig. 4b). The specific activity was constant at high loadings but dropped at low enzyme loading. Presumably, the cross-linking was too high in these solids, resulting in more constrained enzyme conformation with lower activity.

The activity of the immobilized enzyme in **GOx_25@TS-1_Aer** was compared to the free enzyme (Fig. 4c). The results showed a residual activity of *ca.* 50% for the immobilized **GOx**. This activity drop should be attributed to the cross-linking procedure which is known to lower the accessibility to individual active sites (using our kinetic modeling – ESI, Fig. S18† – lower k and higher k_{mO} values were obtained for the aggregated enzymes as compared to the free enzyme). However, entrapped CLEAs were also shown to exhibit higher thermal stability as compared to the free enzyme. Indeed, the time-dependent evolution of the enzymatic activity upon incubation at 45 °C showed a decrease of the activity for the free enzyme (estimated half-life of *ca.* 8 h), whereas the immobilized enzyme showed no sign of deactivation in the same time interval (Fig. 4d).[69]

SEM analysis showed that the immobilization step did not affect the catalyst spherical morphology. Besides, the catalytic

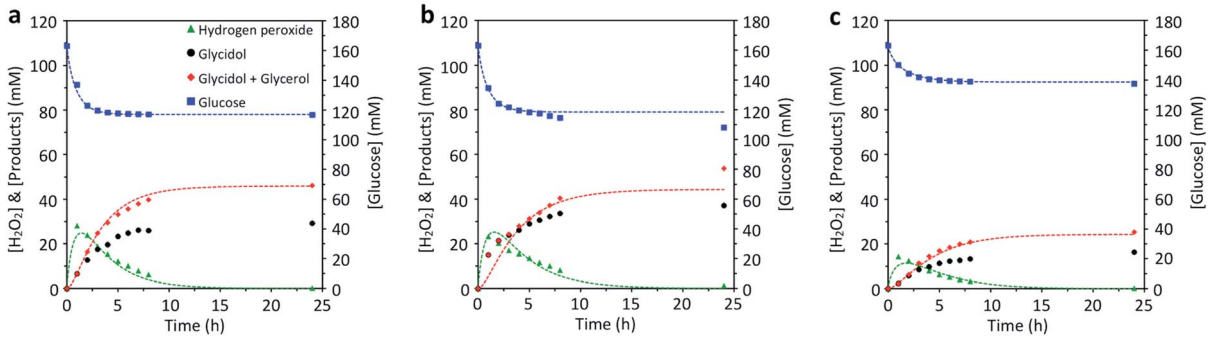

Fig. 5 Chemo-enzymatic epoxidation of allyl alcohol with (a) free **GOx** and **TS-1_Aer**, (b) **GOx_25@TS-1_Aer**, and (c) **GOx_2.5@TS-1_Aer**. The amount of free enzyme in experiment (a) was adjusted so as to have the same enzymatic activity as in the hybrid **GOx_25@TS-1_Aer** catalyst (experiment (b)). Dashed lines represent a fitted mathematical model (see Table S1†). Experimental conditions: $T = 45$ °C, [D-glucose] = 0.16 M, [CATA] = 5 g L^{-1}, [allyl alcohol] = 0.9 M, 24 h reaction time.

activity of **GOx_25@TS-1_Aer** for the Ti-catalyzed conversion of allyl alcohol showed only a *ca.* 20% decrease compared to **TS-1_Aer** (Fig. 3a). This slight drop possibly results from the mass fraction of organics (*ca.* 10% w/w, see Fig. S4†), including small enzyme aggregates, in the hybrid material. This is evidenced by the loss of textural properties in **GOx_25@TS-1_Aer** (external specific surface area = 130 m^2 g^{-1}; $V_P = 0.30$ cm^3 g^{-1}; $V_\mu = 0.09$ cm^3 g^{-1}; see Fig. 1c) as compared to **TS-1_Aer**.

In conditions depicted in Fig. 5 – without addition of H_2O_2 – the inorganic catalyst **TS-1_Aer** is totally inactive for the epoxidation reaction. With **TS-1_Aer** and free **GOx** (Fig. 5a), the chemo-enzymatic cascade reaction took place: without addition of H_2O_2, the epoxide was formed with a yield of 18% (relative to glucose) and 63% selectivity (as estimated by the mass balance, and further confirmed by HPLC). It should be reminded that the selectivity is governed by the instability of the epoxide in the reaction conditions; spontaneous ring-opening is inevitable for long reaction times. Switching to the true hybrid heterogeneous catalyst, **GOx_25@TS-1_Aer** (Fig. 5b), glycidol production reached a value of 37 mM – corresponding to a yield of 23% and a glucose conversion of 34% (69% selectivity for the epoxide). The slight increase in performance as compared to the case where the enzyme is free is possibly due to confinement effect, implying that the H_2O_2 concentration close to the zeolite nanocrystals is higher when using the hybrid and can be consumed faster. The reported glycidol production (mM range) is much higher than the traces reported for a simple grafting of the enzyme on the external surface of **TS-1**.[31] Enzyme leaching was shown to be limited to less than 1% during the one-pot reaction, as demonstrated by a Bradford assay carried out on filtrated reaction medium (after 24 h). The reproducibility of the data presented in Fig. 5b was confirmed by synthesizing a new hybrid catalyst following the whole same protocol and performing the same reaction (Fig. S15†). In the repeated experiment, the glucose conversion reached 28%, whereas the epoxide yield was of 20% (73% selectivity). It can be observed, however, that the H_2O_2 production seems to peak at an early stage of the experiment. This occurs both for the free enzyme and for the hybrid. In fact, **GOx** is known to be irreversibly deactivated by its product H_2O_2,[70] meaning that the epoxidation reaction is not fueled with additional H_2O_2 after a few hours of operation.

The epoxide production obtained with the hybrid catalyst could be tuned by simply changing the enzyme loading in the hybrid catalyst. This is shown by testing the **GOx_2.5@TS-1_Aer** catalyst (Fig. 5c), the latter having a *ca.* 6 times lower enzyme loading (Fig. S13†) and *ca.* 5 times lower specific enzymatic activity (Fig. 4b) compared to **GOx_25@TS1_Aer**. In this case, only 16 mM of glycidol was formed after 24 h (10% yield, 64% selectivity); the glucose conversion was of 16%. The lack of proportionality between the intrinsic **GOx** activity in **GOx_2.5@TS-1_Aer** and **GOx_25@TS-1_Aer** and the corresponding final glucose conversion in the chemo-enzymatic reaction indicates that the

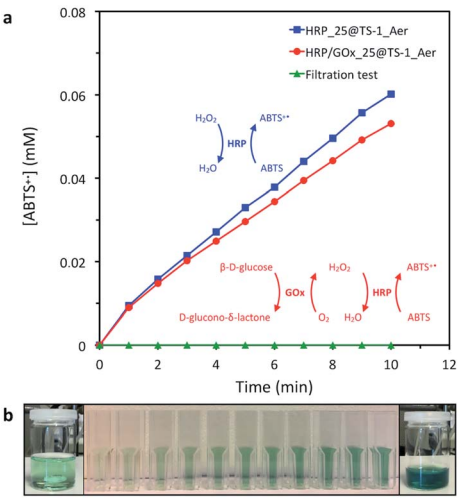

Fig. 6 Colorimetric assay of HRP using ABTS as substrate. (a) Kinetic data for the formation of $ABTS^{+\bullet}$ catalyzed by HRP in **HRP_25@TS-1_Aer** and **HRP/GOx_25@TS-1_Aer**. Filtration tests proved that the enzymatic activity was located in the solid (see one example for **HRP/GOx_25@TS-1_Aer** in the figure, see also Fig. S6†). (b) Evolution of the color of the solution as a function of the production of $ABTS^{+\bullet}$ catalyzed by HRP in **HRP_25@TS-1_Aer**. Experimental conditions: 10 mM citric acid-phosphate pH 6.0, tests carried out at room temperature (*ca.* 23 °C). The detailed experimental procedures are presented in the ESI.†

conversion in the presence of the **GOx_25@TS-1_Aer** catalyst is mostly limited by the oxygen supply, suggesting that even higher epoxide production could be reached by improving the oxygen mass transfer rate in the medium.

In order to demonstrate the applicability of the present strategy to other enzymes, CLEAs of horseradish peroxidase (HRP) were entrapped in **TS-1_Aer** while keeping a nominal enzyme loading of 50 mg g^{-1} (**HRP_25@TS-1_Aer**). A colorimetric assay with 2,2′-azino-bis(3-ethylbenzothiazoline-6-sulfonic acid) (ABTS) and H_2O_2 as substrates demonstrated that the HRP was successfully immobilized in the solid and remained active (Fig. 6, see also Fig. S6a–d†). Moving further, combi-CLEAs made of HRP and **GOx** (75 : 25 w/w, 50 mg g^{-1} nominal enzyme loading) could be effectively formed inside the microspheres (**HRP/GOx_25@TS-1_Aer**). Without external addition of H_2O_2, the reaction occurred, illustrating the possibility to carry out multi-enzymatic cascade reactions (here **GOx** produces H_2O_2 and HRP uses it to oxidize ABTS, see Fig. 6a and S6e–h†). These results confirm that the strategy presented here could be exploited to design multifunctional hybrid solids hosting multi-enzyme systems that could be applied in more complex cascade reactions or for example also as sensors and detection devices.

Conclusions

In conclusion, we report an innovative and effective approach for combining zeolite and enzyme catalysts in the same bifunctional solid and for exploiting them in a one-pot cascade chemo-enzymatic reaction. Leveraging on the aerosol process, hollow zeolite microspheres can be shaped by the aggregation of crystalline nano-building blocks of **TS-1** zeolites cemented by a thin porous silica layer. These one-pot generated hollow microspheres are used as cargos for glucose oxidase. The **GOx** enzyme is loaded in the microsphere and then trapped in the form of cross-linked enzyme aggregates, thereby providing a good control on the enzyme loading, promoting enzyme stability, and preventing enzyme leaching. When this hybrid catalyst is put at work, a cascade chemo-enzymatic reaction is demonstrated: **GOx** produces H_2O_2 *in situ* and the latter is then used by **TS-1** to catalyze the epoxidation of the olefin. The conversion and selectivity obtained with these hybrid catalysts are much higher than the traces of products obtained using a simple grafting on zeolite crystals. This study constitutes one of the rare examples of chemo-enzymatic reaction carried out with a single bifunctional hybrid catalyst, and more precisely the first example of an effective hybrid catalyst based on an enzyme and a zeolite. The catalyst preparation strategy based on the formation of hollow particles is allegedly applicable to other catalytic nano-building units (nanocrystals of zeolites, clays, MOFs, COFs, nanoparticles, *etc.*) to allow their combination with enzymes, multi-enzymes or other biomacromolecules, thus opening new opportunities for the preparation of multifunctional hybrid materials.

Conflicts of interest

There are no conflicts to declare.

Acknowledgements

Authors acknowledge the 'Communauté française de Belgique' for the financial support through the ARC programme (15/20-069). F. Devred and E. Niyigena are acknowledged for the technical and logistical support. V. Smeets is thankful to F. R. S.–F. N. R. S. for his FRIA PhD grant. The authors thank the unité de chimie des nanomatériaux (UCNM) from UNamur for the access to UV-Vis equipment and Hg porosimeter. The authors thank the Francqui Foundation for the chair, which made it possible for Prof. Sanchez to visit Belgium. FEGSEM instrumentation was facilitated by the Institut des Matériaux de Paris Centre (IMPC FR2482) and was funded by UPMC, CNRS and by the C'Nano projects of the Région Ile-de-France. Prof. Patrick Gerin is gratefully acknowledged for providing access to the optical oxygen sensor.

References

1 P. Anastas and N. Eghbali, *Chem. Soc. Rev.*, 2009, **39**, 301–312.
2 R. A. Sheldon, I. W. C. E. Arends and U. Hanefeld, *Green Chemistry and Catalysis*, 2007.
3 F. Rudroff, M. D. Mihovilovic, H. Gröger, R. Snajdrova, H. Iding and U. T. Bornscheuer, *Nat. Catal.*, 2018, **1**, 12.
4 R. Ye, J. Zhao, B. B. Wickemeyer, F. D. Toste and G. A. Somorjai, *Nat. Catal.*, 2018, **1**, 318–325.
5 T. Görbe, K. P. J. Gustafson, O. Verho, G. Kervefors, H. Zheng, X. Zou, E. V. Johnston and J.-E. Bäckvall, *ACS Catal.*, 2017, **7**, 1601–1605.
6 P. O'Brien, D. Lopez-Tejedor, R. Benavente and J. M. Palomo, *ChemCatChem*, 2018, **10**, 4992–4999.
7 H. Huang, C. A. Denard, R. Alamillo, A. J. Crisci, Y. Miao, J. A. Dumesic, S. L. Scott and H. Zhao, *ACS Catal.*, 2014, **4**, 2165–2168.
8 W. Zhang, E. Fernández-Fueyo, Y. Ni, M. van Schie, J. Gacs, R. Renirie, R. Wever, F. G. Mutti, D. Rother, M. Alcalde and F. Hollmann, *Nat. Catal.*, 2018, **1**, 55.
9 M. Frey, L. Seyidova, D. Richard and P. Fongarland, *Catal. Today*, 2019, DOI: 10.1016/j.cattod.2019.04.056.
10 A. Gimbernat, M. Guehl, M. Capron, N. Lopes Ferreira, R. Froidevaux, J.-S. Girardon, P. Dhulster, D. Delcroix and F. Dumeignil, *ChemCatChem*, 2017, **9**, 2080–2084.
11 F. Dumeignil, M. Guehl, A. Gimbernat, M. Capron, N. L. Ferreira, R. Froidevaux, J.-S. Girardon, R. Wojcieszak, P. Dhulster and D. Delcroix, *Catal. Sci. Technol.*, 2018, **8**, 5708–5734.
12 P. N. R. Vennestrøm, C. H. Christensen, S. Pedersen, J.-D. Grunwaldt and J. M. Woodley, *ChemCatChem*, 2010, **2**, 249–258.
13 J. Muschiol, C. Peters, N. Oberleitner, M. D. Mihovilovic, U. T. Bornscheuer and F. Rudroff, *Chem. Commun.*, 2015, **51**, 5798–5811.
14 M. Bohnet, *Ullmann's encyclopedia of industrial chemistry*, Wiley-VCH, Weinheim, Germany, 2003.
15 S. T. Oyama, *Mechanisms in Homogeneous and Heterogeneous Epoxidation Catalysis*, Elsevier, 2011.
16 M. G. Clerici and P. Ingallina, *J. Catal.*, 1993, **140**, 71–83.

17 J. M. Campos-Martin, G. Blanco-Brieva and J. L. G. Fierro, *Angew. Chem., Int. Ed.*, 2006, **45**, 6962–6984.
18 S. B. Bankar, M. V. Bule, R. S. Singhal and L. Ananthanarayan, *Biotechnol. Adv.*, 2009, **27**, 489–501.
19 L. Cao and R. D. Schmid, *Carrier-bound Immobilized Enzymes: Principles, Application and Design*, Wiley-VCH, Weinheim, 1st edn, 2005.
20 F. Hoffmann, M. Cornelius, J. Morell and M. Fröba, *Angew. Chem., Int. Ed.*, 2006, **45**, 3216–3251.
21 C. Chan, L. Sepunaru, S. V. Sokolov, E. Kätelhön, N. P. Young and R. G. Compton, *Chem. Sci.*, 2017, **8**, 2303–2308.
22 R. A. Sheldon and S. van Pelt, *Chem. Soc. Rev.*, 2013, **42**, 6223–6235.
23 J. Huo, J. Aguilera-Sigalat, S. El-Hankari and D. Bradshaw, *Chem. Sci.*, 2015, **6**, 1938–1943.
24 L. van den Biggelaar, P. Soumillion and D. P. Debecker, *Catalysts*, 2017, **7**, 54.
25 M. L. Contente and F. Paradisi, *Nat. Catal.*, 2018, **1**, 452–459.
26 K. S. Rabe, J. Müller, M. Skoupi and C. M. Niemeyer, *Angew. Chem., Int. Ed.*, 2017, **56**, 13574–13589.
27 X. Lian, Y.-P. Chen, T.-F. Liu and H.-C. Zhou, *Chem. Sci.*, 2016, **7**, 6969–6973.
28 M. Filice and J. M. Palomo, *ACS Catal.*, 2014, **4**, 1588–1598.
29 Y. Lin, L. Wu, Y. Huang, J. Ren and X. Qu, *Chem. Sci.*, 2015, **6**, 1272–1276.
30 K. Engström, E. V. Johnston, O. Verho, K. P. J. Gustafson, M. Shakeri, C.-W. Tai and J.-E. Bäckvall, *Angew. Chem., Int. Ed.*, 2013, **52**, 14006–14010.
31 P. N. R. Vennestrøm, E. Taarning, C. H. Christensen, S. Pedersen, J.-D. Grunwaldt and J. M. Woodley, *ChemCatChem*, 2010, **2**, 943–945.
32 X. Zhang, L. Jing, F. Chang, S. Chen, H. Yang and Q. Yang, *Chem. Commun.*, 2017, **53**, 7780–7783.
33 X. Li, X. Cao, J. Xiong and J. Ge, *Small*, 2019, DOI: 10.1002/smll.201902751.
34 D. P. Debecker, *Chem. Rec.*, 2018, **18**, 662–675.
35 V. Smeets, C. Boissière, C. Sanchez, E. M. Gaigneaux, E. Peeters, B. F. Sels, M. Dusselier and D. P. Debecker, *Chem. Mater.*, 2019, **31**, 1610–1619.
36 G. Deo, A. M. Turek, I. E. Wachs, D. R. C. Huybrechts and P. A. Jacobs, *Zeolites*, 1993, **13**, 365–373.
37 V. Smeets, L. Ben Mustapha, J. Schnee, E. M. Gaigneaux and D. P. Debecker, *Mol. Catal.*, 2018, **452**, 123–128.
38 M. G. Clerici, *Kinet. Catal.*, 2015, **56**, 450–455.
39 C. Pagis, A. R. Morgado Prates, D. Farrusseng, N. Bats and A. Tuel, *Chem. Mater.*, 2016, **28**, 5205–5223.
40 D. P. Debecker, S. Le Bras, C. Boissière, A. Chaumonnot and C. Sanchez, *Chem. Soc. Rev.*, 2018, **47**, 4112–4155.
41 C. Boissiere, D. Grosso, A. Chaumonnot, L. Nicole and C. Sanchez, *Adv. Mater.*, 2011, **23**, 599–623.
42 D. P. Debecker, M. Stoyanova, F. Colbeau-Justin, U. Rodemerck, C. Boissière, E. M. Gaigneaux and C. Sanchez, *Angew. Chem., Int. Ed.*, 2012, **51**, 2129–2131.
43 X.-Y. Yang, L.-H. Chen, Y. Li, J. C. Rooke, C. Sanchez and B.-L. Su, *Chem. Soc. Rev.*, 2017, **46**, 481–558.
44 J. Zhou, Z. Hua, W. Wu, Z. Liu, Y. Zhu, Y. Chen and J. Shi, *Dalton Trans.*, 2003, **2011**(40), 12667–12669.
45 A. Dong, Y. Wang, Y. Tang, N. Ren, Y. Zhang and Z. Gao, *Chem. Mater.*, 2002, **14**, 3217–3219.
46 Z. Guo, G. Xiong, L. Liu, P. Li, L. Hao, Y. Cao and F. Tian, *J. Porous Mater.*, 2016, **23**, 407–413.
47 G. Majano, A. Restuccia, M. Santiago and J. Pérez-Ramírez, *CrystEngComm*, 2012, **14**, 5985–5991.
48 L.-H. Chen, X.-Y. Li, G. Tian, Y. Li, J. C. Rooke, G.-S. Zhu, S.-L. Qiu, X.-Y. Yang and B.-L. Su, *Angew. Chem., Int. Ed.*, 2011, **50**, 11156–11161.
49 N. Masoumifard, R. Guillet-Nicolas and F. Kleitz, *Adv. Mater.*, 2018, **30**, 1704439.
50 V. Smeets, E. M. Gaigneaux and D. P. Debecker, *Microporous Mesoporous Mater.*, 2020, **293**, 109801.
51 V. R. R. Marthala, M. Friedrich, Z. Zhou, M. Distaso, S. Reuss, S. A. Al-Thabaiti, W. Peukert, W. Schwieger and M. Hartmann, *Adv. Funct. Mater.*, 2015, **25**, 1832–1836.
52 A. Corma, V. Fornes and F. Rey, *Adv. Mater.*, 2002, **14**, 71–74.
53 C. Niu, M. Liu, X. Gao, X. Ye, Y. Wen, Y. Liu and X. Wang, *ACS Omega*, 2019, **4**, 4397–4404.
54 R. A. Sheldon, *Catalysts*, 2019, **9**, 261.
55 H. Yamaguchi, Y. Kiyota and M. Miyazaki, *Catalysts*, 2018, **8**, 174.
56 D. Jung, M. Paradiso and M. Hartmann, *J. Mater. Sci.*, 2009, **44**, 6747.
57 J. Lee, J. Kim, J. Kim, H. Jia, M. I. Kim, J. H. Kwak, S. Jin, A. Dohnalkova, H. G. Park, H. N. Chang, P. Wang, J. W. Grate and T. Hyeon, *Small*, 2005, **1**, 744–753.
58 A. Thangaraj, M. J. Eapen, S. Sivasanker and P. Ratnasamy, *Zeolites*, 1992, **12**, 943–950.
59 B. M. Reddy, B. Chowdhury and P. G. Smirniotis, *Appl. Catal., A*, 2001, **211**, 19–30.
60 B. Erdem, R. A. Hunsicker, G. W. Simmons, E. D. Sudol, V. L. Dimonie and M. S. El-Aasser, *Langmuir*, 2001, **17**, 2664–2669.
61 G. Berlier, V. Crocellà, M. Signorile, E. Borfecchia, F. Bonino and S. Bordiga, in *Structure and Reactivity of Metals in Zeolite Materials*, ed. J. Pérez Pariente and M. Sánchez-Sánchez, Springer International Publishing, Cham, 2018, pp. 91–154.
62 L. Marchese, E. Gianotti, V. Dellarocca, T. Maschmeyer, F. Rey, S. Coluccia and J. M. Thomas, *Phys. Chem. Chem. Phys.*, 1999, **1**, 585–592.
63 K. Madhusudan Reddy, S. V. Manorama and A. Ramachandra Reddy, *Mater. Chem. Phys.*, 2003, **78**, 239–245.
64 K. Thamaphat, P. Limsuwan and B. Ngotawornchai, *Kasetsart J.: Nat. Sci.*, 2008, **42**, 357–361.
65 S. Pega, C. Boissière, D. Grosso, T. Azaïs, A. Chaumonnot and C. Sanchez, *Angew. Chem., Int. Ed.*, 2009, **48**, 2784–2787.
66 A. Y. Khan, S. B. Noronha and R. Bandyopadhyaya, *Biochem. Eng. J.*, 2014, **91**, 78–85.
67 P. A. Webb, C. Orr and M. I. Corporation, *Analytical methods in fine particle technology*, Micromeritics Instrument Corporation, 1997.
68 R. Schoevaart, M. W. Wolbers, M. Golubovic, M. Ottens, A. P. G. Kieboom, F. van Rantwijk, L. a. M. van der Wielen and R. A. Sheldon, *Biotechnol. Bioeng.*, 2004, **87**, 754–762.
69 R. R. Nair, P. Demarche and S. N. Agathos, *New Biotechnol.*, 2013, **30**, 814–823.
70 K. Kleppe, *Biochemistry*, 1966, **5**, 139–143.